GeoVirtual 2020 September 14-16 Resilience and Innovation

Time-dependent borehole deformation in shale rocks and the influences on in-situ stress inversion

Hongxue Han, Maurice B. Dusseault & Shunde Yin
University of Waterloo, waterloo, Ontario, Canada
Zhuoheng Chen
Geological Survey of Canada, Calgary, Alberta, Canada

ABSTRACT
This paper presents a novel, economical, and prompt method to estimate the in-situ stresses and geomechanical parameters from borehole deformation data, which are determined from four-arm caliper logs. The methodology includes a poro-visco-elastic Finite Element Method simulation to quantify the time-dependent borehole deformation of shale and an optimization approach of the in-situ stresses inversion. It is observed first that the time-dependent borehole deformation is mainly influenced by the visco-elastic properties of the rock; second, that the inverted maximum horizontal in-situ stress for visco-elastic shale rocks is substantially smaller than that of a linear-elastic calculation; and last, the estimate Young's modulus for visco-elastic rocks is much higher than the Young's modulus calculated from linear-elastic rocks.

RÉSUMÉ
Cet article présente une méthode nouvelle, économique et rapide pour estimer les contraintes in-situ et les paramètres géomécaniques à partir de données de déformation de forage, qui sont déterminées à partir de diagraphies d'étrier à quatre bras. La méthodologie comprend une simulation poro-visco-élastique de la méthode des éléments finis pour quantifier la déformation du puits de forage en fonction du temps et une approche d'optimisation de l'inversion des contraintes in situ. On constate tout d'abord que la déformation du forage en fonction du temps est principalement influencée par les propriétés visco-élastiques de la roche; deuxièmement, que la contrainte horizontale in-situ maximale inversée pour les roches schisteuses visco-élastiques est sensiblement inférieure à celle d'un calcul linéaire-élastique; et enfin, le module de Young estimé pour les roches visco-élastiques est beaucoup plus élevé que le module de Young calculé à partir des roches linéaires-élastiques.

1 INTRODUCTION

In-situ stresses measurements and laboratory geomechanics parameter tests generally require a substantial overhead cost and a long waiting time, yet the results may only be available for limited formations in only a few wells in an oilfield. For example, casing shoe leak-off tests are never taken within a producing reservoir and are generally in shale strata. Moreover, properties achieved from the lab are not necessarily those appropriate for in-situ stress change analysis, where mismatched confining stresses must be applied to mimic the in-situ conditions underground.

Therefore, there have been efforts to develop economical empirical methods to estimate in-situ horizontal stresses. The commonly used empirical method in oilfield practice is based on empirical correlations between rock mechanical properties or rock physical properties and the values from geophysical sonic and density logs (Desroches & Kurkjian, 1999; Chang *et al*., 2006; Sinha *et al*., 2008; Najibi *et al*., 2017). In recent years, some efforts have been devoted to the in-situ stress determination from breakouts information (Zhang *et al*., 2018a; Zhang *et al*., 2018b; Zhang *et al*., 2019; Zhang and Yin, 2019; Zhang and Yin, 2020). Such methods require no hydraulic fracturing data; the width and depth of breakouts are the main inputs for this inversion method.

In 2018, Han and Yin (Han and Yin, 2018a; 2018b), developed a method to determine in-situ stresses and rock mechanics properties using borehole deformation data read from four-arm calipers logs. The methodology considers the original borehole size as an unknown parameter to obtain reasonable borehole deformation in the field. Then, the linear elastic analytical calculation, artificial neural network modeling, genetic algorithm method, and probabilistic analysis are integrated to narrow

the uncertainty ranges of the estimated rock mechanical properties and the in-situ stresses from borehole deformation information.

However, in drilling practices of unconventional resources, a shale borehole wall might deform in a time-dependent manner due to a viscous response of the rock. Obvious differences in caliper log measurements between active drilling data and days after drilling using geophysical logs have been observed showing time-dependent borehole wall deformations (Bonner *et al*., 1992). Moreover, a borehole will become non-circular instantaneously after drilling because of stress anisotropy. Research has shown that only 2% of the principal axis length difference in an elliptical borehole geometry can lead to a 5% difference in the minimum horizontal stress (σ_h) calculation and a 10% difference in the maximum horizontal stress (σ_H) calculation (Han *et al*., 2018). Therefore, the conventional circular-borehole-based linear-elastic analytical solutions might not be adequate for inverting stresses from four-arm caliper measurements in actual oilfield practice. A poro-visco-elastic simulation approach is developed using the Finite Element Method (FEM) to quantify the time-dependent borehole deformation and to analyze its influence on the inversion process for in-situ stress estimation.

2 NUMERICAL MODELING OF TIME-DEPENDENT BOREHOLE DEFORMATION IN PORO-VISCO-ELASTIC ROCKS

2.1 Problem Definition

A three-dimensional FEM model for a single-layer circular borehole is developed and used to analyze the poro-visco-elastic deformation of the borehole wall. The model can be conveniently modified to comply with irregular boreholes and multi-layers in future research. The cross-section plane view of the mesh is shown in Figure 1.

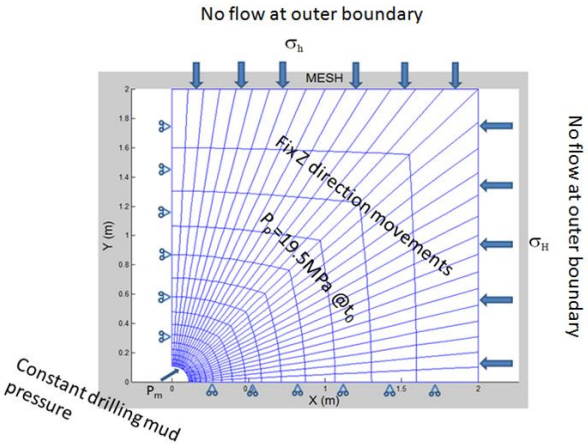

Figure 1. Cross section plane view of mesh with boundary conditions

The model dimension is 2 meters by 2 meters (from borehole center to edges) by 0.02 meters (vertical layer thickness). The original borehole diameter is assumed to be 8.7 inches (0.22 meters). Twenty-node brick elements are employed for the FEM model, as shown in Figure 2. The total number of elements is 450; the total number of nodes is 3378.

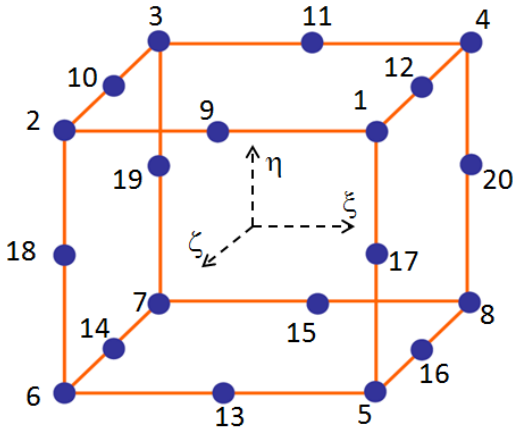

Figure 2. A 20-node brick element of FEM

2.2 Governing and Constitutive Equations

The governing equations for the equilibrium of forces with body forces ignored are shown as follows:

$$\frac{\partial \sigma_{xx}}{\partial x}+\frac{\partial \tau_{yx}}{\partial y}+\frac{\partial \tau_{zx}}{\partial z}=0 \quad [1]$$

$$\frac{\partial \sigma_{yy}}{\partial y}+\frac{\partial \tau_{xy}}{\partial x}+\frac{\partial \tau_{zy}}{\partial z}=0 \quad [2]$$

$$\frac{\partial \sigma_{zz}}{\partial z}+\frac{\partial \tau_{xz}}{\partial x}+\frac{\partial \tau_{yz}}{\partial y}=0 \quad [3]$$

where i =x,y,z, j= x,y,z, σ stands for normal stress, τ stands for shear stress. By combining the above governing equations, the generalized Hooke's Law, and the strain-displacement relations, the Navier's equation without the body force term can be written as follows:

$$(\lambda+G)\left(\frac{\partial^2 u_x}{\partial x^2}+\frac{\partial^2 u_y}{\partial x \partial y}+\frac{\partial^2 u_z}{\partial x \partial z}\right)+G\left(\frac{\partial^2 u_x}{\partial x^2}+\frac{\partial^2 u_x}{\partial y^2}+\frac{\partial^2 u_x}{\partial z^2}\right)=0 \quad [4]$$

$$(\lambda+G)\left(\frac{\partial^2 u_x}{\partial x \partial y}+\frac{\partial^2 u_y}{\partial y^2}+\frac{\partial^2 u_z}{\partial y \partial z}\right)+G\left(\frac{\partial^2 u_y}{\partial x^2}+\frac{\partial^2 u_y}{\partial y^2}+\frac{\partial^2 u_y}{\partial z^2}\right)=0 \quad [5]$$

$$(\lambda+G)\left(\frac{\partial^2 u_x}{\partial x \partial z}+\frac{\partial^2 u_y}{\partial y \partial z}+\frac{\partial^2 u_z}{\partial z^2}\right)+G\left(\frac{\partial^2 u_z}{\partial x^2}+\frac{\partial^2 u_z}{\partial y^2}+\frac{\partial^2 u_z}{\partial z^2}\right)=0 \quad [6]$$

where λ and G are the elastic constants of the material (λ is Lamé's first parameter, G is Lamé's second parameter or the shear modulus), and, u_x, u_y, u_z are displacements in the x, y, and z directions respectively.By applying Galerkin's method, the element elastic stiffness matrix is described as follows:

$$\boldsymbol{K}=\iiint \boldsymbol{B}^T\boldsymbol{D}\boldsymbol{B}dxdydz \quad [7]$$

The solution in global matrix form is described as

$$\mathbf{[M][u]=[f^u]} \quad [8]$$

where **M** is elastic stiffness matrix, **u** is the vector of displacements, and $\mathbf{f}^u$ is the vector of nodal loads. The

FEM formulation for the poro-visco-elasticity theory can be written as the following:

$$\begin{bmatrix} \mathbf{M(t)} & -\mathbf{C(t)} \\ \mathbf{C(t)}^{\mathrm{T}} & \mathbf{S(t)} + \Delta t\mathbf{H} \end{bmatrix} \begin{Bmatrix} \mathbf{u}_1 \\ \mathbf{p}_1 \end{Bmatrix} = \begin{bmatrix} \mathbf{0} & \mathbf{0} \\ \mathbf{C(t)}^{\mathrm{T}} & \mathbf{S(t)} \end{bmatrix} \begin{Bmatrix} \mathbf{u}_0 \\ \mathbf{p}_0 \end{Bmatrix} + \begin{Bmatrix} (\mathbf{f}^u) \\ \Delta t\mathbf{f}^p \end{Bmatrix} \quad [9]$$

where **M(t)**, **S(t),** and **C(t)** are time-dependent elastic stiffness, flow capacity, and coupling matrices respectively, **H** is flow stiffness, Δt is the time increment. The explicit expressions of the above matrices are as follows:

$$\mathbf{M(t)} = \int_V \mathbf{B}^{\mathrm{T}}\mathbf{D(t)}\mathbf{B}\mathrm{d}V \quad [10]$$

$$\mathbf{H} = \frac{k}{\mu}\int_V (\boldsymbol{\nabla}\mathbf{N}_p)^{\mathrm{T}}(\boldsymbol{\nabla}\mathbf{N}_p)\mathrm{d}V \quad [11]$$

$$\mathbf{S(t)} = \int_V \mathbf{N}_p^{\mathrm{T}}\left[\frac{1-\emptyset}{K_s} + \frac{\emptyset}{K_f} - \frac{1}{(3K_s)^2}\mathbf{i}^{\mathrm{T}}\mathbf{D(t)}\mathbf{i}\right]\mathbf{N}_p\mathrm{d}V \quad [12]$$

$$\mathbf{C(t)} = \int_V \left(\mathbf{B}^{\mathrm{T}}\mathbf{i}\mathbf{N}_p - \mathbf{B}^{\mathrm{T}}\mathbf{D(t)}\frac{\mathbf{i}}{3K_s}\mathbf{N}_p\right)\mathrm{d}V \quad [13]$$

where $\mathbf{N}_p$ is shape function, K, K_f and K_s are the bulk moduli of the matrix, fluid, and solid skeleton respectively, $\mathbf{i}^{\mathrm{T}}$=[1,1,1,0,0,0], and **D** is the elasticity matrix expressed using Young's modulus E and Poisson's ratio ν.

2.3 Boundary and Initial Conditions

Boundary conditions and initial conditions for the proposed FEM are:

- the borehole wall is subjected to mud pressure.
- the right boundary is subjected to the far field maximum horizontal stress.
- the top boundary is subjected to the far field minimum horizontal stress.
- the left boundary is comprised of rollers (no left and right displacement) and is traction free.
- the bottom boundary is comprised of rollers (no up and down displacement) and is traction free.
- Z direction is movement free for all nodes (plane strain).
- the outer boundaries are free of fluid flow.
- the borehole mud pressure is constant.
- no fluid flow at time zero.
- fluid flow starts at the first time-step.

The model mimics plane strain 2-D problems and can be verified by corresponding 2-D plane strain analytical solutions.

2.4 Model Verification

2.4.1 Verification of visco-elastic FEM modeled borehole deformation

The generalized Kelvin model (as shown in Figure 3) was used to verify the borehole deformations of stiff shale rocks. The analytical equations to calculate shorter diameter (u_{rrA}) and longer diameter (u_{rrB}) are described in equations 14 and 15:

$$u_{rrA} = \frac{r}{2G(t)} \times ((\upsilon - 1) \times (3\sigma_H - \sigma_h) + p_m) \quad [14]$$

$$u_{rrB} = \frac{r}{2G(t)} \times ((\upsilon - 1) \times (3\sigma_h - \sigma_H) + p_m) \quad [15]$$

where u_{rrA} is the shorter diameter, u_{rrB} is the longer diameter, r is original borehole radius, ν is Poisson's ratio, σ_H is the maximum horizontal stress, σ_h is the minimum horizontal stress, p_m is borehole mud pressure, $G(t)$ is the time-dependent shear relaxation modulus.

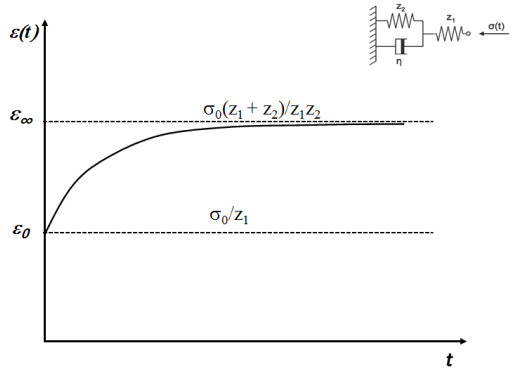

Figure 3. Strain-time plot of a generalized Kelvin model
(z_1 and z_2 are spring constants, η is dashpot viscosity, σ_0 is stress at time zero.)

The FEM visco-elastic borehole deformation simulation using parameters listed in Table 1, and the analytical calculations through equations 14 and 15 using the same parameters, have been conducted. The magnitudes of deformations (or the displacements) at the borehole wall along the shorter axis direction, u_{rrA}, and magnitudes of the deformations at the borehole wall along the longer axis direction, u_{rrB}, are plotted in Figure 4. The figure shows that the analytical calculation verified the FEM visco-elastic borehole deformation simulation very well.

Table 1. Characteristics of tested soils

Parameter	Value
Young's modulus, E (GPa)	3.2
Poisson ratio, ν	0.2
Minimum horizontal stress, σ_h (MPa)	23
Maximum horizontal stress, σ_H (MPa)	43
Rock solid bulk modulus, K_s (GPa)	39
Spring constant of Kelvin model, z_1 (MPa)	3.2
Spring constant of Kelvin model, z_2 (MPa)	3.2
Dashpot viscosity, η (Pa·s)	10^{14}
Mud pressure, P_m (MPa)	14
Assumed original borehole diameter, 2r (inch)	8.7

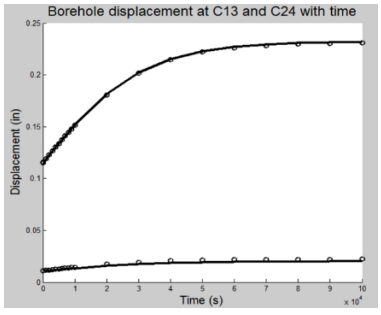

Figure 4. Borehole deformations of FEM modeling and analytical calculations
(*Black lines represent FEM modeling results; small circles represent analytical solutions; the upper curve indicates the borehole wall displacements along the shorter axis; the lower curve indicates the borehole wall displacements along the longer axis.)*

2.4.2 Stress verification of the poro-elastic FEM model

The radial displacements of circular openings due to pore pressure change is a function of the difference of the anisotropic stresses that are applied orthogonal to the openings and is difficult to be solved analytically (Carter and Booker, 1982; Detournay and Cheng, 1988). However, the radial effective stress (σ'_{rr}) and the tangential effective stress ($\sigma'_{\theta\theta}$) around a circular opening (such as a borehole) can be calculated analytically according to the poro-elastic theory. The equations are described as

$$\sigma'_{rr} = \left(1-\frac{r^2}{R^2}\right)\left(\frac{\sigma'_H+\sigma'_h}{2}\right) + \left(1+\frac{3r^4}{R^4}-\frac{4r^2}{R^2}\right)\left(\frac{\sigma'_H-\sigma'_h}{2}\right)\cos(2\theta) + \frac{r^2}{R^2}(p_m-\alpha p_p) \quad [16]$$

$$\sigma'_{\theta\theta} = \left(1+\frac{r^2}{R^2}\right)\left(\frac{\sigma'_H+\sigma'_h}{2}\right) - \left(1+\frac{3r^4}{R^4}\right)\left(\frac{\sigma'_H-\sigma'_h}{2}\right)\cos(2\theta) - \frac{r^2}{R^2}(p_m-\alpha p_p) \quad [17]$$

where r is the borehole radius, R is distance from borehole center, σ'_{rr} is the effective radial stress normal to the borehole wall, $\sigma'_{\theta\theta}$ is the effective tangential stress around borehole, σ'_H is the effective far-field maximum horizontal stress, σ'_h is the effective far-field minimum horizontal stress, p_m is the borehole mud pressure, p_p is formation pore pressure, and θ is the angle from maximum horizontal stress direction.

Using the parameters listed in Table 2, both analytical calculations and FEM simulations were conducted. The scenario of zero mud pressures was demonstrated. The effective tangential stresses and the effective radial stresses around the borehole area at time zero are illustrated in Figures 5 and 6.

Table 2. Input parameters for verifying poro-elastic FEM modeling

Parameter	Value
Young's modulus, E (GPa)	32
Poisson ratio, ν	0.2
Biot coefficient, α	0.54
Minimum effective horizontal stress, σ_h (MPa)	26
Maximum effective horizontal stress, σ_H (MPa)	43
Rock solid bulk modulus, K_s (GPa)	39
Dashpot viscosity, η (Pa·s)	10^{14}
Pore pressure, P_p (MPa)	19.5
Mud pressure, P_m (MPa)	0
Permeability, k (m^2)	10^{-15}
Porosity, ϕ	0.07
Fluid viscosity, μ (cp)	10^{-3}
Assumed original borehole diameter, 2r (inch)	8.7

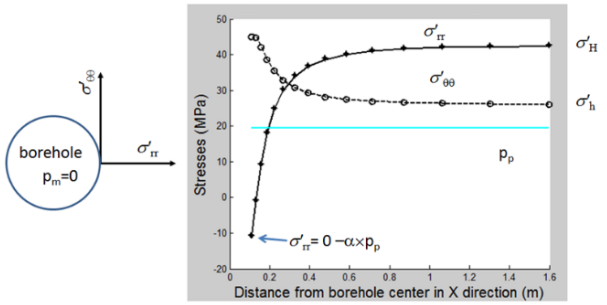

Figure 5. Horizontal stresses near borehole along X direction

In Figure 5, the solid line represents the FEM simulated radial effective stresses around the borehole at distances away from the borehole center along the X axis; the dashed line represents FEM simulated tangential effective stresses around borehole at distances away from the borehole center along the X axis. The stars are the calculated radial effective stresses around the borehole using the analytical equation 16; and, the small circles are the calculated tangential effective stresses around borehole using the analytical equation 17. The analytical solutions verify the FEM calculations very well.

Similarly, in Figure 6, the radial and tangential stresses around borehole at distances away from borehole center along the Y direction, are very well verified by the analytical solutions.

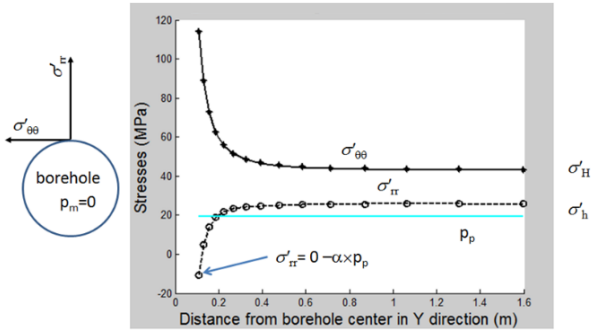

Figure 6. Horizontal stresses near borehole along Y direction

2.5 Simulation Results of Poro-visco-elastic Borehole Beformation

The FEM model for poro-visco-elastic borehole wall deformation has been run using the parameters listed in Table 3. The results of borehole wall radial deformations with time after drilling are shown in Figure 7. It is observed that the linear-elastic and poro-elastic displacements contribute very little to the time-dependent borehole deformations, whereas the visco-elastic property of the rock is the major cause of the borehole creep. The borehole wall creep in this example (with assumed rock visco-elastic properties and in-situ stresses) terminates at ~2 hours (7000 seconds) after drilling. The final displacements are almost twice the initial linear elastic displacements (the instantaneous deformation) in both longer and shorter axis directions.

Table 3. Input parameters for poro-visco-elastic FEM modeling

Parameter	Value
Young's modulus, E (GPa)	32
Poisson ratio, ν	0.2
Minimum horizontal stress, σ_h (MPa)	26
Maximum horizontal stress, σ_H (MPa)	43
Rock solid bulk modulus, K_s (GPa)	39
Spring constant of Kelvin model, z_1 (MPa)	32
Spring constant of Kelvin model, z_2 (MPa)	32
Dashpot viscosity, η (Pa·s)	10^{14}
Pore pressure, p_0 (MPa)	19.5
Mud pressure, p_m (MPa)	14
Permeability, k (m^2)	10^{-15}
Porosity, ϕ	0.07
Fluid viscosity, μ (cp)	10^{-3}
Assumed original borehole diameter, r (inch)	8.7

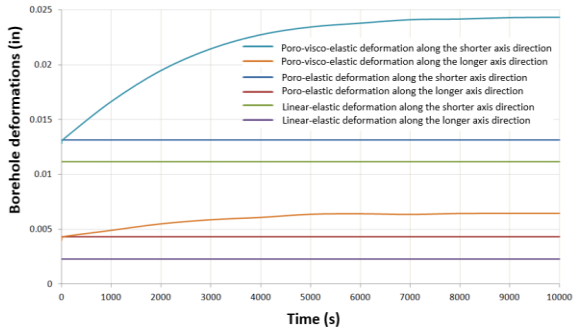

Figure 7. Borehole wall creep at directions of longer and shorter axis

Table 4 lists the magnitudes of the linear-elastic, poro-elastic and poro-visco-elastic FEM simulations of borehole diameters with time. The borehole diameters remain unchanged with time in linear-elastic simulations. The poro-elastic simulation results of borehole wall deformation are just slightly (0.0034 inches) larger than the linear-elastic simulation results at the beginning. It is also observed from the poro-elastic simulation results that although there is no further pressure variation on the borehole wall (except at the initial time step), the borehole wall deforms with time because of effective stresses change in the near wellbore area. However, the magnitude of this change is only ~10^{-3} inches, and it makes sense that it is often neglected in field practice.

Table 4. Borehole diameters variations with time

Time (s)	Linear elastic		Poro-elastic		Poro-visco-elastic	
	C_{13} (inch)	C_{24} (inch)	C_{13} (inch)	C_{24} (inch)	C_{13} (inch)	C_{24} (inch)
0	8.6954	8.6777	8.6920	8.6743	8.6920	8.6743
0.1	8.6954	8.6777	8.6918	8.6741	8.6918	8.6741
1	8.6954	8.6777	8.6915	8.6738	8.6915	8.6738
10	8.6954	8.6777	8.6914	8.6737	8.6915	8.6738
100	8.6954	8.6777	8.6914	8.6737	8.6913	8.6731
1000	8.6954	8.6777	8.6914	8.6737	8.6902	8.6667
10000	8.6954	8.6777	8.6914	8.6737	8.6871	8.6513

3 IN-SITU STRESS INVERSION METHODOLOGY

Theoretically, the longer and shorter diameters of an elliptical borehole can be determined through either analytical calculations or through FEM simulations as describe in the previous section, should Young's modulus, Poisson's ratio, original borehole size, borehole pressure, two horizontal stresses, relaxation moduli, and timing of rock creep be known. However, the inverse calculation of the in-situ stresses and the rock mechanical parameters from the measured borehole diameters might result in multiple solutions because the number of unknowns is larger than the number of solution equations.

Therefore, optimization approaches for the inversion of in-situ stresses and the rock mechanical parameters from borehole deformation data are applied to find the best estimation. The objective functions of the optimization methods can be defined as: the length difference of the longer axis, the length difference of the shorter axis, and the difference between the ratio of the measured shorter axis length over the measured longer axis length and the ratio of the calculated shorter axis length over the calculated longer axis length.

Generally, in multi-objective optimization problems, weighted-sum methods are adopted (Augusto *et al.,* 2013; Kim and Weck, 2019). If the objective functions for the in-situ stresses and rock mechanical properties inversion from the borehole deformations data are composed of only the differences between the measured and calculated borehole diameters, these objective functions will have similar magnitudes that are in the range of 0-1 (typically in the magnitude of 10^{-2}).

However, if the magnitude of the functions are quite different (for example, the difference of Young's modulus or the difference of minimum in-situ stress is several MPa or GPa, which is quite different from the objective function value of the borehole diameters), then a normalized weighted-sum multi-objective will be required, which is defined as:

$$\min \qquad \sum_{i=1}^{n} w_i \times |(D_i - C_i)| \qquad [18]$$

where n is the total number of objectives; D_i is the calculated value of the i^{th} objective, C_i is the measured value of the i^{th} objective, and w_i is the corresponding normalized weight for the i^{th} objective.

In this research, a Matlab™ function "fmincon", which stands for "find minimum of constrained nonlinear multi-variable function", will be used to find the best fitness for the normalized weighted-sum multi-objective functions.

The overall workflow for the poro-visco-elastic borehole deformation FEM modeling and the in-situ stresses inversion optimization is shown in Figure 8. The input of the known parameters and the constraints on the unknown parameters will be determined according to the availability of the parameters and the other information related to the research area.

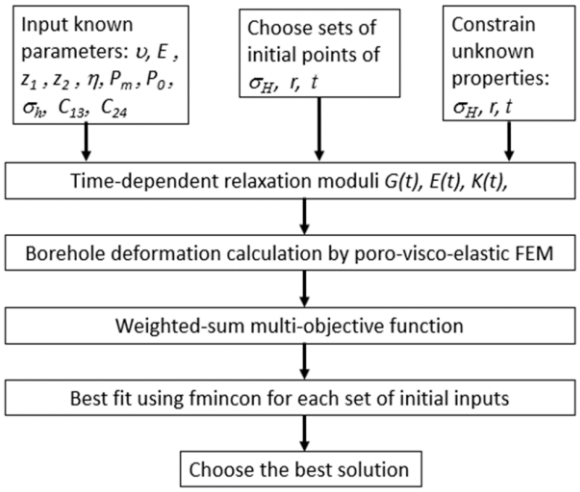

Figure 7. Flow chart of poro-visco-elastic modeling and time-dependent stress inversion

4 SHALE CREEP EFFECTS ON IN-SITU STRESS INVERSION

Rock creep behavior influences the measured borehole longer diameter (C_{13}) and shorter diameter (C_{24}), which will in turn, affect the determination of the in-situ stresses calculated from these measurements. In order to demonstrate the effects of time-dependent borehole deformation on the determination of in-situ stresses, visco-elastic modeling based on the data listed in Table 5 was conducted following the workflow described in Figure 8.

Table 5. Parameters for time-dependent borehole deformation

Parameter	Value
Young's modulus, *E* (GPa)	32
Poisson ratio, ν	0.2
Spring constant of Kelvin model, z_1 (GPa)	32
Spring constant of Kelvin model, z_2 (GPa)	32
Dashpot viscosity, η (Pa·s)	10^{14}
Mud pressure, p_m (MPa)	14
Minimum horizontal stress, σ_h (MPa)	26
Bit size, (inch)	8.5
Measured longer diameter (inch)	8.6954
Measured shorter diameter (inch)	8.6777
Range of original borehole size, *2r* (inch)	8.7-8.8
Range of maximum horizontal stress, σ_H (MPa)	35-50
Range of timing of after drilling (hour)	0-72

A normalized weighted-sum multi-objective function is considered and described in the following form.

$$\text{Min}\quad 0.2\times\frac{|(C13-8.6954)|}{0.1}+0.2\times\frac{|(C24-8.6777)|}{0.1}+0.2\times\frac{|(C24/C13-0.998)|}{0.1}+0.4\times\frac{|(\sigma_h-26)|}{10} \quad [19]$$

where C_{13} is the calculated longer axis length, C_{24} is the calculated shorter axis length, and σ_h is the calculated minimum horizontal in-situ stress. Matlab™ function "fmincon" was used to find the best fitness. The calculation results are shown in Table 6.

Table 6. Results from normalized weighted-sum multi-objective function

Initial input	Objective Function	C_{13} inch	C_{24} inch	σ_H MPa	σ_h MPa	Original hole inch	Timing hour
1	7.11E-05	8.6954	8.6777	36	26	8.7063	0.76
2	3.57E-03	8.6970	8.6777	35	26	8.7102	36.00
3	3.57E-03	8.6970	8.6777	35	26	8.7102	49.98
4	0.00354	8.6967	8.6775	35	26	8.7099	36.51

Among the four initial inputs, the first input has the lowest objective function value, which gives the estimated maximum horizontal stress of 36 MPa based on the 8.71 original borehole size and the measurement of calipers are around 45 minutes after drilling. Table 7 lists the inverted maximum horizontal stress from the linear-elastic model and the visco-elastic model. It is observed that the visco-elastic model estimates a substantially smaller maximum in-situ stress than the linear-elastic calculations.

Table 7. Shale creep effects on the maximum horizontal stress inversion

σ_H (elastic model) MPa	σ_H (visco-elastic model) Mpa	Time (after drilling) hour
43	36	0.76

5 CREEP EFFECTS ON YOUNG'S MODULUS ESTIMATION

The shale creep effects on the determination of Young's modulus was demonstrated using data from a well (00-06-26-064-01W6-0) that was drilled through the Duvernay Formation in Western Canada Sedimentation Basin. Non-breakout sections were identified around depth of 3876 meters. Borehole deformation from the four-arm caliper logging data is listed in Table 8. The ranges for the unknown parameters are listed in Table 9.

Table 8. Available wells suitable for in-situ stress determination

Depth (m)	Bit size (inch)	Shorter Diameter (C_{24}) (inch)	Longer Diameter (C_{13}) (inch)
3876	6	6.0476	6.1081

Table 9. Ranges of unknown parameters for calculation

2r inch	*E* GPa	σ_h MPa	σ_H MPa
6.05-6.60	1-60	69-93	93-156

Table 10 shows the linear-elastic modeling results. The estimated minimum horizontal stress gradient is 21 kPa/m. It agrees well with the reported far-field minimum horizontal

principal stress gradient in the Duvernay Formation near Fox Creek, Alberta with highest and lowest values of 22 and 17 kPa/m (Shen *et al.*, 2018). There is no maximum horizontal stress magnitude reported for the area.

Table 10. Linear-elastic modeling results

Bit inch	Hole inch	*E* GPa	σ_h MPa	σ_H MPa	σ_h gradient kPa/m
6	6.12	22	80	137	21

The estimated Young's modulus from the linear-elastic model is 22 GPa. In order to demonstrate the creep effects on the estimation of the Young's modulus, the workflow was repeated but using a visco-elastic model under the same maximum and minimum horizontal stresses and the original borehole size. The calculated Young's modulus is 45 GPa at 24 hours after drilling (Table 11). Young's modulus calculated from the visco-elastic model is much larger than the linear elastic calculations under the same in-situ stresses and the original borehole sizes.

Table 11. Shale creep effects on the calculation of Young's modulus

E (elastic model) GPa	*E* (visco-elastic model) GPa	Timing (after drilling) hour
22	45	24

6 CONCLUSIONS

An integrated workflow to quantify the time-dependent borehole deformation in shale rocks and to inverse the in-situ stresses and geomechanical parameters were developed by combining a poro-visco-elastic FEM simulation and an optimization approach.

It is observed that the time-dependent borehole deformation is mainly influenced by the visco-elastic properties of the rock; the pore pressure diffusion effects have a negligible influence on the time-dependent borehole deformations.

For visco-elastic rocks, from a geomechanics point of view, the inverted in-situ stress is substantially smaller than that of linear-elastic calculations; the estimate Young's modulus is much higher than that calculated from linear-elastic models.

REFERENCES

Augusto, O., Fouad, B. and Caro, S. (2013). A new method for decision making in multi-objective optimization problems. *Sociedade Brasileira de Pesquisa Operacional* 32(3): 331-369.

Bonner, S., Clark, B., Holenka, J., Voisin, B., Dusang, J., Hansen, R., White, J. and Walsgrove, T. (1992). Logging while drilling: a three-year perspective. *Oilfield Review* 4(3):4-21.

Carter, J. P. and Booker, J.R. (1982). Elastic consolidation around a deep circular tunnel. *International Journal of Solids and Structures* 18(12): 1059-1074.

Chang, C., Zoback, M. D. and Khaksar, A. (2006). Empirical relations between rock strength and physical properties in sedimentary rocks. *Journal of Petroleum Science and Engineering* 51(3-4): 223–237.

Desroches, J., and Kurkjian, A. L. (1999). Applications of wireline stress measurements. *SPE Reservoir Evaluation & Engineering* 2(5):451-461.

Detournay, E. and Cheng, A. H-D. (1988). Poroelastic response of a borehole in a non-hydrostatic stress field. *International Journal of Rock Mechanics and Mining Science & Geomechanics Abstracts* 25: 171-182.

Han, H. X., Yin, S., and Aadnoy, B. S. (2018). Impact of elliptical borehole on in-situ stress estimation from leak-off test data. *Petroleum Science* 15(4): 794-800.

Han, H. X., and Yin, S. (2018a), Determination of in-situ stress and geomechanical properties from borehole deformation. *Energy* 11(1): 131.

Han, H. X., and Yin, S. (2018b), In-situ stress inversion in Liard Basin, Canada, from caliper logs. *Petroleum*, In press.

Kim, Y. I., and Weck, O. (2019). Adaptive weighted sum method for multi-objective optimization. *Structural and Multidisciplinary Optimization* 31:105-116.

Najibi, A. R., Ghafoori, M., Lashkaripour, G. R., and Asef, M. R. (2017). Reservoir geomechanical modeling: in-situ stress, pore pressure, and mud design. *Journal of Petroleum Science and Engineering* 151: 31–39.

Shen, L., Schmitt, D.R., and Haug, K. (2018). Measurements of the states of in-situ stress for the Duvernay Formation near Fox Creek, West-Central Alberta. AER/AGS Report 97. *Alberta Energy Regulators*, Calgary, Alberta, Canada.

Sinha, B. K., Wang, J., Kisra, S., Li, J., Pistre, V., Bratton, T., Sanders, M., and Jun, C., (2008). Estimation of formation stresses using borehole sonic data. Paper SPWLA-2008-F, presented at *49th Annual Logging Symposium*, Austin, Texas, USA.

Zhang, H., Yin, S., and Aadnoy, B. S. (2018a). Poroelastic modeling of borehole breakouts for in-situ stress determination by Finite Element Method. *Journal of Petroleum Science and Engineering* 162: 674-684.

Zhang, H., Yin, S., and Aadnoy, B. S. (2018b). Finite-element modeling of borehole breakouts for in situ stress determination. *International Journal of Geomechanics* 18(12): 04018174.

Zhang, H., Yin, S., and Aadnoy, B. S. (2019). Numerical investigation of the impacts of borehole breakouts on breakdown pressure. *Energies* (12): 888.

Zhang, H., and Yin, S. (2019). Inference of in situ stress from thermoporoelastic borehole breakouts based on artificial neural network. *International Journal for Numerical and Analytical Methods in Geomechanics* 43(16):1-19.

Zhang, H., and Yin, S. 2020. Poroelastoplastic borehole modeling by tangent stiffness matrix method. *International Journal of Geomechanics* 20(3): 04020010.